Spatially separated HOMO-LUMO sites in highly intra- and inter-plane crystalline g-C$_3$N$_4$ photocatalyst for exceptional H$_2$ generation

Binbin Zhao [a], Jiachao Xu [a], Duoduo Gao [a], Feng Chen [a], Xuefei Wang [a], Tao Liu [b], Xinhe Wu [c,*], Huogen Yu [a,b,**]

[a] State Key Laboratory of Silicate Materials for Architectures and School of Chemistry, Chemical Engineering and Life Sciences, Wuhan University of Technology, Wuhan 430070, PR China
[b] Laboratory of Solar Fuel, Faculty of Materials Science and Chemistry, China University of Geosciences, Wuhan 430074, PR China
[c] Hubei Key Laboratory of Pollutant Analysis and Reuse Technology, College of Chemistry and Chemical Engineering, Hubei Normal University, Huangshi 435002, PR China

ARTICLE INFO

ABSTRACT

Spatially separated HOMO-LUMO sites in the highly crystalline g-C$_3$N$_4$ can vastly facilitate the rapid transfer and separation of photogenerated charges to greatly improve its photocatalytic performance, which remains a great challenge to be achieved. In this study, the highly intra- and inter-plane crystalline g-C$_3$N$_4$ (*c*-CN) with the spatially separated HOMO-LUMO sites is explicitly produced through a moderate Na-modulated strategy to efficiently promote the directional transfer and separation of photoinduced charges. As a result, the optimized *c*-CN1.0 photocatalyst exhibits exceptional H$_2$-evolution performance (313.5 μmol h^{-1}, AQE = 13.38 %), which is ca. 14.3 times of the bulk g-C$_3$N$_4$. The excellent hydrogen-generation efficiency of *c*-CN photocatalyst is mainly ascribed to the synergism of high intra- and inter-layer crystallization of g-C$_3$N$_4$ and spatially separated HOMO-LUMO sites, which can vastly boost the directional transfer and effective separation of photoexcited electrons and holes. This research may open novel avenues to construct other photocatalysts with high efficiency.

1. Introduction

Considering the current serious environmental pollution and energy crisis, water splitting by using photocatalysts is regarded as an attractive pathway to produce clean and renewable H$_2$ energy [1–7]. Beyond the numerous inorganic semiconductors for photocatalytic hydrogen evolution (such as TiO$_2$ [8–13], CdS [14–16], ZnIn$_2$S$_4$ [17–20], etc.), graphitic carbon nitride (g-C$_3$N$_4$) is recognized as a highly attractive photocatalyst because of its nontoxicity, facile preparation and suitable bandgap [21–24]. Typically, various nitrogen-containing organics (melamine, dicyandiamide, urea, etc.) can act as precursors to produce the conventional g-C$_3$N$_4$ material via a facile high-temperature calcination [25–29]. However, the resulting g-C$_3$N$_4$ material usually presents poor crystallinity due to the drastic shock of small molecules during the calcination process, such as precursors and small intermediates. In this case, abundant internal and surface defects are produced in the final g-C$_3$N$_4$ structure, which can cause the random transfer of photoexcited

electrons and holes, resulting in their rapid recombination (Fig. 1A). In consequence, the conventional g-C$_3$N$_4$ material typically displays extremely low photocatalytic hydrogen-production efficiency. Hence, it is imperative and valuable to efficiently promote the migration and separation of photoexcited charges to enhance the photocatalytic H$_2$-production efficiency of conventional g-C$_3$N$_4$ material.

Recently, various highly crystalline g-C$_3$N$_4$ materials have been widely constructed to facilitate the rapid transfer of photogenerated charges to enhance their photocatalytic activity [30–33]. Herein, improving the crystallinity of g-C$_3$N$_4$ materials can vastly reduce various defects and boost the formation of ordered structure to decrease the recombination rate of photoexcited electrons and holes, leading to their prominently enhanced photocatalytic performance (Fig. 1B). For instance, Guo et al. [34] developed the highly crystalline porous g-C$_3$N$_4$ photocatalyst with outstanding activity through an initial hydrothermal reaction of melamine at 180 °C and the following calcination of hydrothermal product and KCl at 550 °C. We also constructed the highly

---

crystalline g-C$_3$N$_4$ photocatalyst with exceptional hydrogen-generation performance by heating the mixture of dicyandiamide and CH$_3$COONa [35]. Guo et al. [36] synthesized the in-plane highly ordered g-C$_3$N$_4$ nanosheets via calcining the mixed melamine and NaCl for high-efficiency photocatalytic CH$_3$SH mineralization. As shown in the above results, the transfer of photogenerated charges can be efficiently boosted via increasing the crystallinity of g-C$_3$N$_4$ material, realizing the excellent photocatalytic efficiency. On the other hand, the spatial distribution of highest occupied molecular orbitals (HOMO) and lowest unoccupied molecular orbitals (LUMO) is another crucial ingredient that greatly affects the photocatalytic efficiency, which is tightly related to the migration and separation of photoexcited charges [37,38]. However, owing to the overlapped distribution of HOMO and LUMO in the conventional crystalline g-C$_3$N$_4$, the photoexcited electrons and holes can randomly transfer into the same locations (Fig. 1B), which can extremely restrain the separation of photoinduced charges, leading to the confined increase of photocatalytic performance. Therefore, it is quite believed that if the HOMO and LUMO sites of g-C$_3$N$_4$ photocatalyst can be effectively separated in the highly crystalline g-C$_3$N$_4$ to boost the directional migration of photoexcited electrons and holes, the exceptional H$_2$-evolution performance is unavoidably realized. Regrettably, the related researches about spatial separation of HOMO and LUMO sites in the highly crystalline g-C$_3$N$_4$ have been rarely reported.

In this article, the spatially separated HOMO-LUMO sites can be realized in the highly intra- and inter-plane crystalline g-C$_3$N$_4$ (c-CN) to induce the directional transfer of photogenerated electrons and holes via a moderate Na-modulated strategy, resulting in the exceptional photocatalytic hydrogen-production activity. Briefly, the mixed melamine and sodium chloride are sintered to produce highly intra-layer crystalline g-C$_3$N$_4$ (i-CN) material, which is further treated through the hydrochloric acid solution to enhance its inter-layer crystallization to produce c-CN. Herein, the intercalated Na ions in c-CN material can be regulated through HCl solutions to form the spatially separated HOMO-LUMO sites in c-CN material (Fig. 1C). As a result, photocatalytic tests indicate that the prepared c-CN1.0 material displays the maximal hydrogen-evolution activity (313.5 μmol h^{-1}, AQE = 13.38 %), which is ca. 14.3 times of the bulk g-C$_3$N$_4$. Herein, the high intra- and inter-layer crystallization of g-C$_3$N$_4$ photocatalyst and spatially separated HOMO-LUMO sites can synergistically boost the directional migration and effective separation of photoexcited electrons and holes, thus leading to its distinctly enhanced photocatalytic hydrogen-generation activity. This research may offer new routes to design other high-performance photocatalysts for various applications.

2. Experimental section

2.1. Preparation of traditional bulk g-C$_3$N$_4$

The traditional bulk g-C$_3$N$_4$ was produced via calcining pure melamine precursor. Briefly, 3.0 g of pristine melamine precursor was calcined at 550 °C for 4 h (5 °C/min) under N$_2$ atmosphere to produce bulk g-C$_3$N$_4$.

2.2. Preparation of highly intra- and inter-plane crystalline g-C$_3$N$_4$ (c-CN)

The highly intra- and inter-plane crystalline g-C$_3$N$_4$ was fabricated via a moderate Na-modulated strategy. In detail, 3.0 g of melamine was mixed with 6.0 g of NaCl in a mortar. Then, the above mixture was heated at 630 °C for 2 h with a ramp rate of 5 °C/min under N$_2$ atmosphere. After naturally cooling down, the resultant solid was washed with pure water and dried at 60 °C to gain the highly intra-layer crystalline g-C$_3$N$_4$ (i-CN). Subsequently, 500 mg of the above i-CN sample was added to the hydrochloric acid solution (20 mL) and heated at 80 °C for 2 h. After filtering, washing and desiccating, the obtained sample was the highly intra- and inter-plane crystalline g-C$_3$N$_4$ (c-CN). To investigate the effect of HCl concentration on the photocatalytic hydrogen-generation efficiency of c-CN, the HCl concentration was adjusted as 0.1, 0.2, 0.5, 1.0, 2.0 and 3.0 mol L^{-1}, and the produced photocatalyst was marked as c-CNx, where the x refers to the HCl concentration.

3. Results and discussion

3.1. Strategy for the synthesis of highly intra- and inter-plane crystalline g-C$_3$N$_4$ (c-CN)

In this work, the highly intra- and inter-plane crystalline g-C$_3$N$_4$ (c-CN) photocatalyst with spatially separated HOMO-LUMO sites is constructed through a moderate Na-modulated strategy, as shown in Fig. 2A. Compared to the synthesis of conventional g-C$_3$N$_4$ via calcining pristine melamine precursor, NaCl salt is initially mixed with melamine precursor and further heated at 630 °C. Herein, the NaCl salt can boost the fine polymerization of melamine precursor to form heptazine units and the following ordered arrangement of intra-plane heptazine units, realizing the successful generation of highly intra-layer crystalline g-C$_3$N$_4$ (i-CN) material. XRD results can be used to strongly prove the successful preparation of i-CN material. As displayed in Fig. 2B, the conventional bulk g-C$_3$N$_4$ presents two characteristic XRD peaks at 13.0°
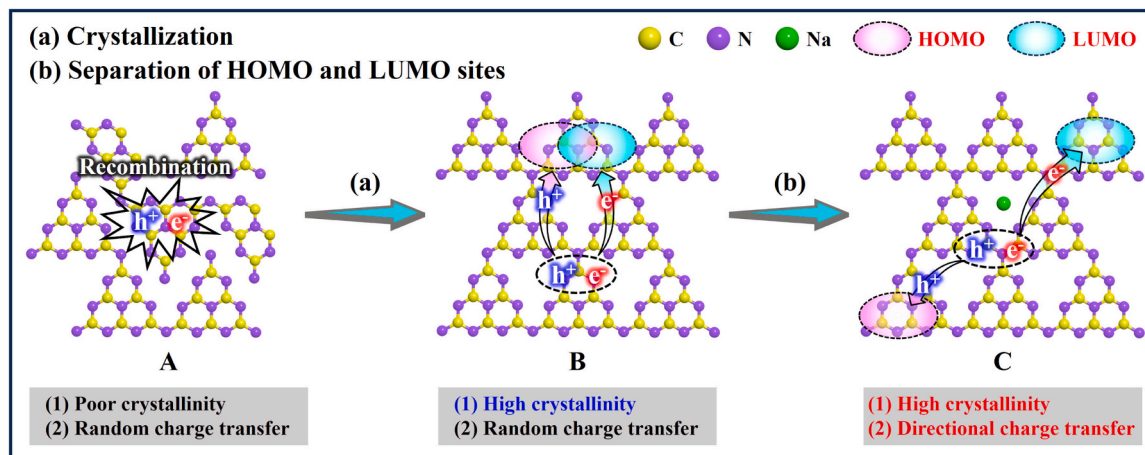
Fig. 1. Schematic illustration of the strategy for boosting the photocatalytic performance of g-C$_3$N$_4$: (a) crystallization and (b) separation of HOMO and LUMO sites, and corresponding g-C$_3$N$_4$ photocatalyst: (A) traditional bulk g-C$_3$N$_4$, (B) conventional crystalline g-C$_3$N$_4$ and (C) c-CN.
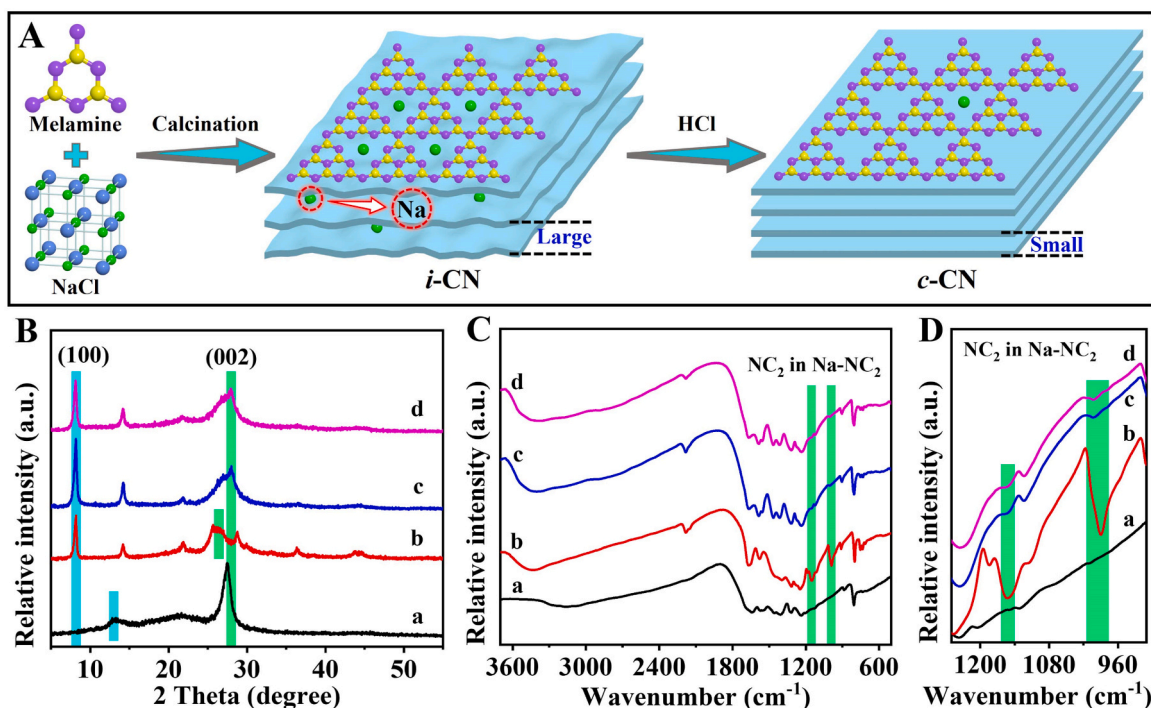
Fig. 2. (A) Synthetic illustration of *i*-CN and *c*-CN, (B) XRD patterns and (C, D) FTIR spectra: (a) bulk g-C₃N₄, (b) *i*-CN, (c) *c*-CN0.1 and (d) *c*-CN1.0.

and 27.4°, indexed to the (100) and (002) crystal facets, which originates from the intra-layer repeated organization of melem units and inter-layer stacking of aromatic planes, respectively [39–41]. Nevertheless, the (100) peak of bulk g-C₃N₄ is extremely weak, revealing its poor intra-plane crystallinity. Compared to traditional bulk g-C₃N₄, the (100) characteristic peak of prepared *i*-CN shifts from 13.0° to 8.2°, which is possibly attributed to the Na⁺ residue from NaCl salt [36]. Moreover, the *i*-CN sample displays an obviously enhanced intensity of (100) diffraction peak, distinctly verifying its high intra-plane crystallinity [36]. However, compared to the (002) peak at 27.4° of conventional bulk g-C₃N₄, the (002) peak of obtained *i*-CN shifts from 27.4° to 26.4° and exhibits a distinctly decreased intensity (Fig. 2B), indicating its increased inter-plane distance and reduced inter-layer crystallinity, which may be due to the abundant Na⁺ residue. Herein, the abundant Na⁺ residue in the prepared *i*-CN is not conducive to the regular stacking of conjugated aromatic planes, leading to its weak inter-layer crystallization. Besides, FTIR results are employed to clearly confirm the intercalation of abundant Na⁺ into *i*-CN. As visualized in Fig. 2C and 2D, the bulk g-C₃N₄ clearly exhibits several peaks at 3000–3400, 1180–1700 and 806 cm⁻¹, which originate from the N-H groups, CN heterocyclic ring, and s-triazine, respectively, in line with previous reports [42,43]. After the NaCl salt is introduced to the synthesis of *i*-CN, the resulting *i*-CN displays a new absorption peak at 2182 cm⁻¹, which is allocated to the cyano groups [44,45]. Notably, in comparison to bulk g-C₃N₄, two characteristic absorption peaks at 1153 and 990 cm⁻¹ are clearly identified in the produced *i*-CN material, which are ascribed to the asymmetric and symmetric vibrations of the NC₂ bond in Na-NC₂ group, respectively [36,46], demonstrating the abundant Na⁺ residue in the *i*-CN structure. Based on the aforementioned investigations, it is reasonable to conclude that the intercalated Na⁺ in the *i*-CN structure can vastly affect its inter-layer crystallization.

Herein, HCl solution is employed to reduce the amount of disordered Na ions in the *i*-CN structure to further promote the inter-layer crystallization (Fig. 2A). The reduced Na⁺ content can be confirmed by FTIR results. As shown in Fig. 2C and 2D, the absorption peaks at 1153 and 990 cm⁻¹ of prepared *c*-CN materials exhibit significantly reduced intensity, clearly revealing the decreased Na⁺ content in the *c*-CN

structure. Furthermore, as demonstrated by XRD data (Fig. 2B), it can be seen that compared to *i*-CN, the (002) diffraction peaks of obtained *c*-CN shift from 26.4° to 28.0°, strongly indicating the reduced inter-layer distance, which is due to the increased interaction of between neighboring layers. In addition, after the *i*-CN is coped via hydrochloric acid solution, the produced *c*-CN materials present stronger (002) peaks than *i*-CN (Fig. 2B), suggesting their increased intra-plane crystallinity. Besides, the strong (100) peaks of *c*-CN materials are still identified in their XRD pattern. The aforementioned XRD data can distinctly verify the high intra- and inter-layer crystallization of prepared *c*-CN photocatalysts. For comparison, the traditional bulk g-C₃N₄ material is also treated through HCl solution under the same conditions as synthesis of *c*-CN. The corresponding XRD and FTIR results prove that the bulk g-C₃N₄ material exhibits negligible change before and after the treatment of HCl solution (Fig. S1). As mentioned above, it is reasonable to conclude that the highly intra- and inter-plane crystalline g-C₃N₄ material can be availably constructed via the moderate Na-modulated strategy.

3.2. Characterizations of highly intra- and inter-plane crystalline g-C₃N₄ (c-CN)

The successful production of *c*-CN material can be strongly confirmed through TEM images. As shown in Fig. 3A, the produced *c*-CN1.0 displays a typical lamellar structure, which is well matched with widely covered g-C₃N₄. HRTEM images are applied to verify the high intra- and inter-layer crystallization of *c*-CN1.0. As evidenced by Fig. 3B and C, the lattice spacings of 1.04 and 0.32 nm are obviously identified in HRTEM results of *c*-CN1.0, which are indexed to the (100) and (002) planes of g-C₃N₄, respectively, apparently illustrating the high intra- and inter-layer crystallization of prepared *c*-CN1.0 material [36,47]. Additionally, HAADF-STEM and EDS mapping results of *c*-CN1.0 display that the C and N elements are well dispersed in the same distribution region (Fig. 3D-D₃). Notably, a small amount of Na⁺ also homogeneously coexists with C and N elements, distinctly proving the intercalation of few Na ions in the *c*-CN1.0 structure, which can be further confirmed through the ICP-OES result. The actual content of Na element is identified to be 0.015 wt % in the *c*-CN1.0 material by ICP-OES result.
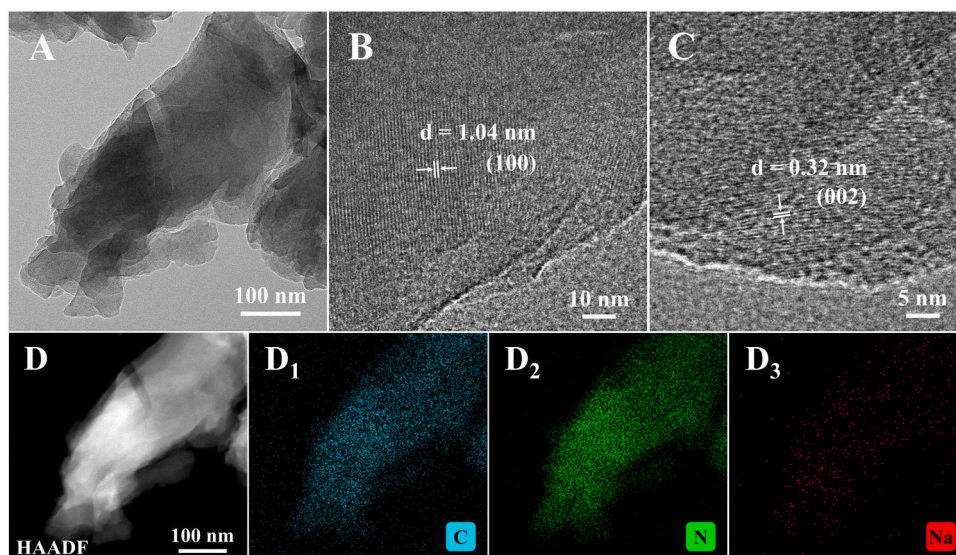
Fig. 3. (A) TEM, (B, C) HRTEM, (D) HAADF-STEM, and (D$_1$-D$_3$) EDS mapping images of *c*-CN1.0.

FESEM and BET are further conducted to investigate the morphology and specific surface area of the prepared *c*-CN1.0 sample. As visualized in Fig. S2 and S3, the traditional bulk g-C$_3$N$_4$ exhibits a seriously agglomerated morphology, and its corresponding S$_{BET}$ is quite low (7.1 m^2 g^{-1}), in line with widely covered works [48–50]. However, after NaCl is introduced for synthesizing *i*-CN, as shown in Fig. S2 and S3, the resulting *i*-CN still shows a severely aggregated structure with a slightly decreased S$_{BET}$ (5.6 m^2 g^{-1}) compared to bulk g-C$_3$N$_4$. After the *i*-CN is further coped via hydrochloric acid solution, the size of resulting *c*-CN1.0 is clearly decreased compared to bulk g-C$_3$N$_4$ and *i*-CN, while its

S$_{BET}$ is increased to be 13.9 m^2 g^{-1} (Fig. S2 and S3), which is beneficial for the photocatalytic H$_2$-production reaction.

XPS is further utilized to analyze the chemical states of various elements, which is displayed in Fig. 4. As revealed by Fig. 4A, it is obvious that all g-C$_3$N$_4$ materials include C, N and O elements, well matched with wide researches [51,52]. For the C element (Fig. 4B), the obvious XPS signals at 284.8 and 288.1 eV of various g-C$_3$N$_4$ materials can be related to the C-C and N=C-N$_2$, respectively [53,54]. The XPS spectra of N element are presented in Fig. 4C, and the XPS peaks at 398.5, 400.1 and 401.1 eV can be allocated to the C-N=C, N-C$_3$ and N-H, respectively
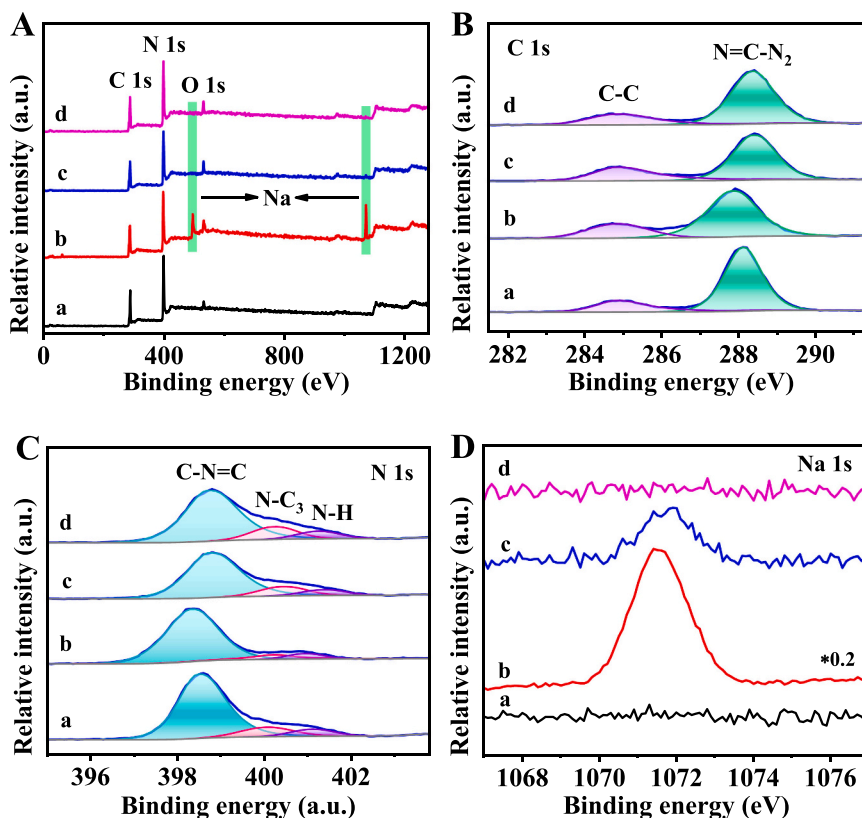

Fig. 4. (A) XPS survey spectra, (B) C 1 s, (C) N 1 s and (D) (the *0.2 represents that the intensity of Na 1 s peak in *i*-CN is weakened by 0.2 times.) Na 1 s high-resolution XPS spectra of various samples: (a) bulk g-C$_3$N$_4$, (b) *i*-CN, (c) *c*-CN0.1 and (d) *c*-CN1.0.

[55,56]. The above XPS results strongly prove the successful preparation of various g-C$_3$N$_4$ materials. In addition, as visualized in Fig. 4D, the *i*-CN exhibits a strong Na 1 s signal compared to traditional bulk g-C$_3$N$_4$, distinctly indicating that the Na$^+$ from NaCl salt can be abundantly intercalated into the *i*-CN structure, which is in line with its FTIR result (Fig. 2C and 2D). After the *i*-CN is treated via 0.1 mol L^{-1} hydrochloric acid solution, the intensity of Na 1 s peak in the produced *c*-CN0.1 material is clearly reduced (Fig. 4D), illustrating the decrease of intercalated Na$^+$ amount. With the further increase of HCl concentration, the signal of Na 1 s cannot be identified in the resulting *c*-CN1.0 (Fig. 4D), which is due to the low content of inserted Na ions. Actually, the intercalated Na$^+$ in the *c*-CN1.0 material can be obviously proved through the FTIR, TEM and ICP-OES results. As shown in above investigation, it is believed that the *c*-CN material can be formed via the moderate Na-modulated strategy. UV–vis spectra are employed to disclose the light-harvesting ability of diverse g-C$_3$N$_4$ materials. As exhibited in Fig. S4, the absorption edge of traditional bulk g-C$_3$N$_4$ is about 463 nm, in line with widely reported works [57,58]. The absorption edge of *i*-CN material exhibits a clearly red shift (ca. 468 nm) compared to bulk g-C$_3$N$_4$, which may be due to the residue of abundant Na ions. After the *i*-CN is coped via 0.1 mol L^{-1} HCl, the absorption edge of produced *c*-CN displays a blue shift (458 nm) due to the decrease of Na$^+$ content, as visualized in Fig. S4. With increasing HCl concentration, the absorption edge of resulting *c*-CN1.0 further shifts to 453 nm because of the further decline of intercalated Na$^+$ amount. In addition, the optical graphs of various g-C$_3$N$_4$ materials are well consistent with their UV–vis spectra, which are visualized in Fig. S4.

3.3. Photocatalytic performance and mechanism

The photocatalytic H$_2$-production tests were utilized to assess the photocatalytic performance of various g-C$_3$N$_4$ materials (Fig. 4). The traditional bulk g-C$_3$N$_4$ material exhibits a low photocatalytic hydrogen-production rate (21.9 μmol h^{-1}) because of its severely agglomerated structure and the rapid recombination of photoinduced charges. However, the photocatalytic H$_2$-evolution rate of *i*-CN material is quite low (0.9 μmol h^{-1}), which is mainly attributed to the massive Na$^+$ residue. Herein, the abundant and disordered Na ions in the *i*-CN structure can act as recombination centers and thus cause the random and rapid recombination of photogenerated carriers. After the *i*-CN is treated by 0.1 mol L^{-1} HCl solution, the obtained *c*-CN0.1 photocatalyst achieves a distinctly improved H$_2$-production performance of 101.1 μmol h^{-1}. With the further increase of HCl concentration (1.0 mol L^{-1}), the resulting *c*-CN1.0 material reaches the maximal photocatalytic H$_2$-generation rate (313.5 μmol h^{-1}, AQE = 13.38 %), which is about 14.3 times of the bulk g-C$_3$N$_4$ sample. The excellent H$_2$-production rate of the *c*-CN1.0 photocatalyst is superior to the majority of highly crystalline g-C$_3$N$_4$ photocatalysts (Table S1). In addition, as shown in Fig. 5B, the *c*-CN1.0 photocatalyst exhibits outstanding stability during four cycling H$_2$-evolution tests.

The above photocatalytic tests reveal that the present *c*-CN materials exhibit splendid photocatalytic activity for H$_2$ production. Hence, it is imperative to elucidate the photocatalytic hydrogen-generation mechanism of the current *c*-CN material. First, the TR-PL spectra are utilized to verify the efficient transfer and separation of photoinduced charges in *c*-CN material. As visualized in Fig. S5A and Table S2, the *c*-CN1.0 photocatalyst presents an obviously decreased average lifetime (τ_a = 11.01 ns) in comparison to traditional bulk g-C$_3$N$_4$ material (τ_a = 14.43 ns), revealing the significantly facilitated transfer and separation of photogenerated charges, which can be further confirmed via the photoelectrochemical tests. As shown in Fig. S5B and S5C, the *c*-CN1.0 material displays a higher photocurrent and a smaller semicircle radius than those of bulk g-C$_3$N$_4$ sample, revealing its promoted migration and separation of photoinduced carriers [59–61]. Based on the above analysis, it can be concluded that the transfer and separation of photoexcited electrons and holes can be vastly boosted in the present *c*-CN photocatalyst.

Additionally, it is well known that the electronic structure of g-C$_3$N$_4$ material tightly correlates with the migration and separation of photoinduced charges. Therefore, it is necessary to investigate the distribution of HOMO and LUMO in the highly intra- and inter-plane crystalline g-C$_3$N$_4$. As displayed in Fig. 6A and B, the HOMO and LUMO are overlapped and located at the whole structure of the traditional crystalline g-C$_3$N$_4$. Herein, the photoexcited charges can easily migrate to the same sites and thus lead to their rapid recombination. In contrast, the current *c*-CN obviously exhibits the spatially separated HOMO-LUMO sites, as shown in Fig. 6D and E. In this case, the photoexcited electrons and holes can orientationally transfer to the spatial LUMO and HOMO sites, respectively, vastly inhibiting the recombination of photoexcited carriers, which greatly contributes to the photocatalytic hydrogen-generation performance of the present *c*-CN material. In addition to the migration and separation of photogenerated charges in the internal structure of g-C$_3$N$_4$, the interfacial transfer and separation of photogenerated charges are important for the photocatalytic activity, which can be investigated by the work functions. As shown in Fig. 6C and F, the work function of *c*-CN (Φ = 5.33 eV) is larger than that of traditional crystalline g-C$_3$N$_4$ (Φ = 4.79 eV), which is closer to the work function of H$_2$-evolution Pt (Φ = 5.65 eV) cocatalyst. Herein, as displayed in Fig. 6I, the Schottky barrier at the Pt/*c*-CN interface is significantly lower than that at the Pt/crystalline g-C$_3$N$_4$ interface, which is favorable to efficient electron migration from g-C$_3$N$_4$ to Pt cocatalyst. The aforementioned results obviously reveal that the migration and separation of photogenerated charges can be distinctly boosted in the current *c*-CN with spatially separated HOMO-LUMO sites.

Femtosecond transient absorption spectroscopy (fs-TAS) is employed to investigate the photogenerated carrier dynamics, as visualized in Fig. 7. It is obvious that the negative signals at 420 nm are observed in all samples, which is ascribed to the ground-state bleach (GSB) [62].
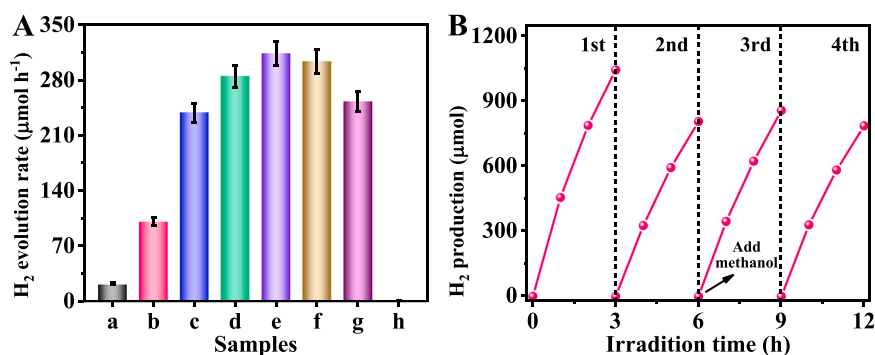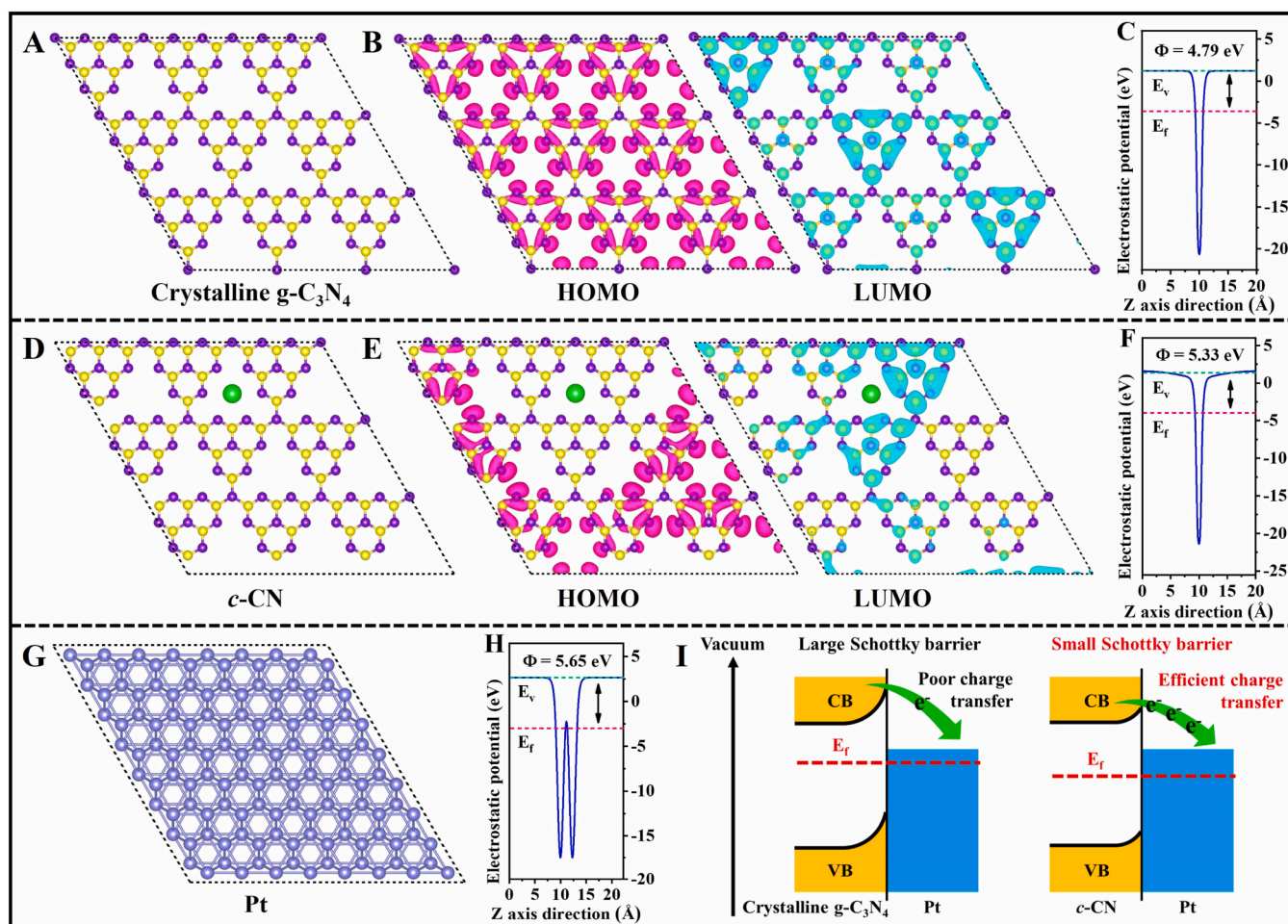

Fig. 5. (A) The photocatalytic hydrogen-generation rate of various photocatalysts: (a) bulk g-C$_3$N$_4$, (b) *c*-CN0.1, (c) *c*-CN0.2, (d) *c*-CN0.5, (e) *c*-CN1.0, (f) *c*-CN2.0, (g) *c*-CN3.0 and (h) *i*-CN, and (B) Cycling runs for photocatalytic H$_2$ evolution of *c*-CN1.0.

Fig. 6. (A, D and G) Structure model for DFT calculations, (B, E) their corresponding HOMO and LUMO, and (C, F and H) calculated electrostatic potentials of (A-C) crystalline g-C$_3$N$_4$, (D-F) *c*-CN and (G, H) Pt, and (I) Graphic diagram for the formation of Schottky barrier in Pt/crystalline g-C$_3$N$_4$ and Pt/*c*-CN.

Typically, the GSB signals closely correlate with the number of photo-induced electrons [63]. In comparison to Pt/bulk g-C$_3$N$_4$ (Fig. 7A, B), the GSB signal intensity of Pt/*c*-CN1.0 is clearly enhanced, manifesting that more photogenerated electrons are produced, which is attributed to the rapid migration of photogenerated electrons from *c*-CN1.0 to Pt cocatalyst. Moreover, the decay kinetics of GSB signals in the Pt/bulk g-C$_3$N$_4$ and Pt/*c*-CN1.0 are fitted by the bi-exponential formulas and displayed in Fig. 7C and F. It is obvious that the decay time of Pt/*c*-CN1.0 (9.53 ps) is significantly shorter than that of Pt/bulk g-C$_3$N$_4$ (17.32 ps), distinctly indicating the fast extraction of photogenerated electrons from *c*-CN1.0 to Pt cocatalyst, which is beneficial for the following H$_2$-evolution reactions. The above fs-TAS results can be further proved through TR-PL and photoelectrochemical data (Fig. S6, Table S1).

According to the above investigations, a convincing photocatalytic hydrogen-evolution mechanism of the *c*-CN with spatially separated HOMO-LUMO sites is proposed and exhibited in Fig. 8. Under light illumination, the photoexcited electrons and holes are produced in the *c*-CN internal structure. The high intra- and inter-plane crystallization of g-C$_3$N$_4$ photocatalyst can distinctly promote the rapid transfer of photoinduced charges in the interior structure of g-C$_3$N$_4$. Moreover, benefiting from the spatial distribution of HOMO-LUMO sites, the photoinduced electrons and holes can directionally migrate to LUMO and HOMO regions in the *c*-CN, respectively, realizing the effective transfer and separation of photoinduced charges. Subsequently, the photoinduced electrons can rapidly transfer from *c*-CN to Pt for the subsequent hydrogen-evolution reactions, while the photogenerated holes participate in the oxidation reaction of the sacrificial agent.

Consequently, owing to the directional migration and separation of photoexcited electrons and holes, the current *c*-CN achieves the splendid photocatalytic hydrogen-evolution activity.

4. Conclusions

To summarize, the highly intra- and inter-plane crystalline g-C$_3$N$_4$ (*c*-CN) material with the spatially separated HOMO-LUMO sites has been successfully constructed via a moderate Na-modulated strategy to efficiently promote the directional transfer and separation of photoexcited charges. Herein, the high intra- and inter-layer crystallization of g-C$_3$N$_4$ photocatalyst and spatially separated HOMO-LUMO sites can synergistically boost the directional migration and effective separation of photoexcited electrons and holes, inhibiting the rapid recombination of photoinduced charges. As a result, photocatalytic experiments indicate that the optimized *c*-CN1.0 photocatalyst exhibits exceptional H$_2$-evolution performance (313.5 μmol h^{-1}, AQE = 13.38 %), which is ca. 14.3 times of the bulk g-C$_3$N$_4$ material. This research emphasizes a moderate Na-modulated strategy to simultaneously improve the high intra- and inter-layer crystallization of g-C$_3$N$_4$ and form its spatially separated HOMO-LUMO sites, which may reveal new insights to design other photocatalysts with excellent activity.

CRediT authorship contribution statement

Huogen Yu: Writing – review & editing, Supervision, Resources, Funding acquisition, Conceptualization. **Xuefei Wang:** Validation,
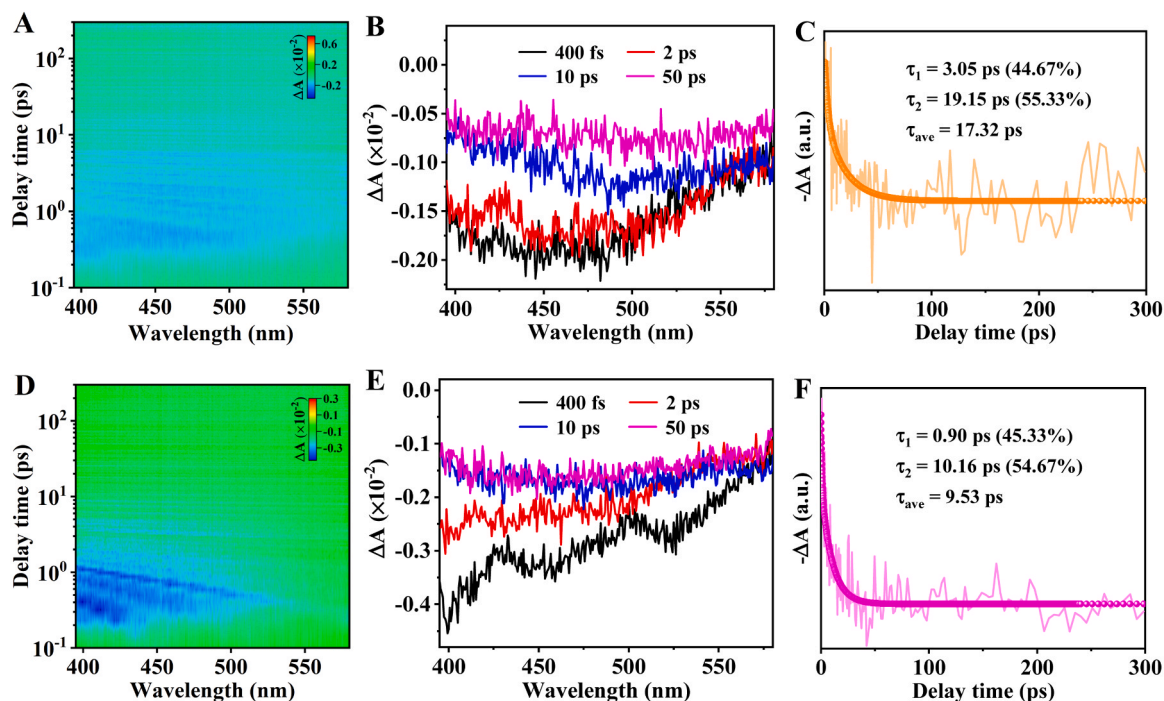
Fig. 7. (A, D) The pseudocolor plots, (B, E) transient absorption signals measured with 325 nm excitation, and (C, F) the corresponding fs-TAS decay curves at 420 nm within 300 ps of (A-C) Pt/bulk g-C$_3$N$_4$ and (D-F) Pt/c-CN1.0.
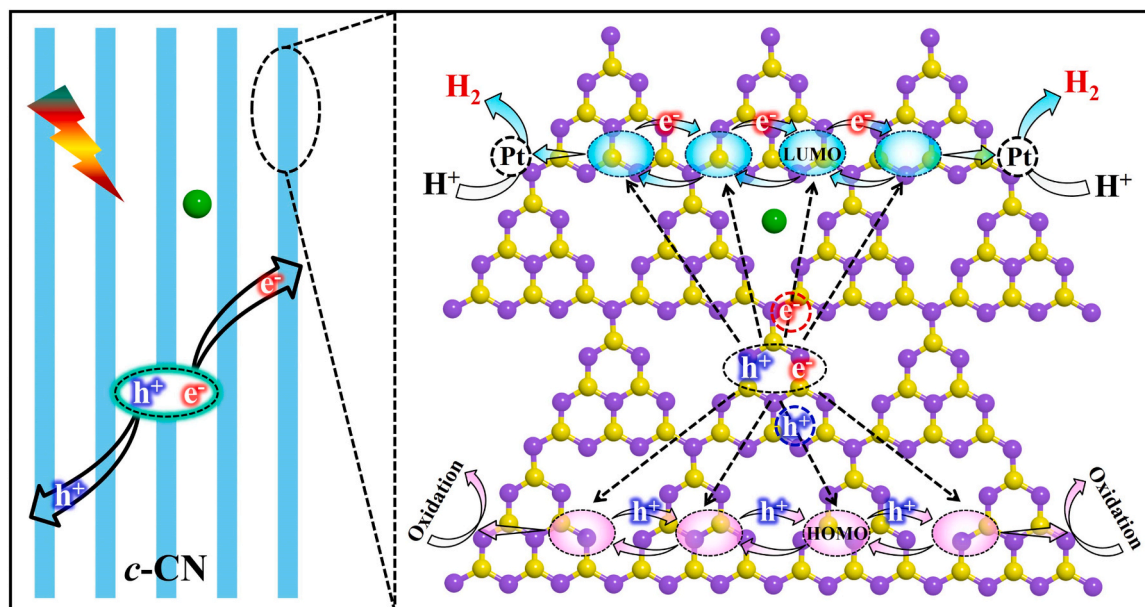

Fig. 8. Proposed photocatalytic hydrogen-production mechanism of the c-CN material.

Project administration. **Feng Chen:** Supervision, Conceptualization. **Duoduo Gao:** Software. **Jiachao Xu:** Visualization. **Binbin Zhao:** Writing – original draft, Methodology, Investigation, Data curation. **Tao Liu:** Resources, Validation. **Xinhe Wu:** Funding acquisition, Resources, Supervision, Writing – review & editing.

Declaration of Competing Interest

The authors declare that they have no known competing financial interests or personal relationships that could have appeared to influence the work reported in this paper.

Data Availability

Data will be made available on request.

University PA230101).

Appendix A. Supporting information

Supplementary data associated with this article can be found in the online version at doi:10.1016/j.apcatb.2024.124215.

References

[1] S. Wang, Z. Ai, X. Niu, W. Yang, R. Kang, Z. Lin, A. Waseem, L. Jiao, H.-L. Jiang, Linker engineering of sandwich-structured metal–organic framework composites for optimized photocatalytic H_2 production, Adv. Mater. 35 (2023) 2302512.

[2] W. Zhong, J. Xu, X. Zhang, J. Zhang, X. Wang, H. Yu, Charging d-orbital electron of ReS_{2+x} cocatalyst enables splendid alkaline photocatalytic H_2 evolution, Adv. Funct. Mater. 33 (2023) 2302325.

[3] S. Liu, K. Wang, M. Yang, Z. Jin, Rationally designed $Mn_{0.2}Cd_{0.8}S@CoAl$ LDH S-scheme heterojunction for efficient photocatalytic hydrogen production, Acta Phys. Chim. Sin. 38 (2022) 2109023.

[4] C. Li, J. Wang, L. Tong, Y. Wang, P. Zhang, M. Zhu, H. Dong, Recent progress and challenges of photocatalytic CO_2 conversion into value-added multi-carbon products, Coord. Chem. Rev. 502 (2024) 215623.

[5] X. Li, Y. Chen, Y. Tao, L. Shen, Z. Xu, Z. Bian, H. Li, Challenges of photocatalysis and their coping strategies, Chem. Catal. 2 (2022) 1315–1345.

[6] W. Zhong, D. Gao, P. Wang, X. Wang, H. Yu, Accelerating hydroxyl desorption by swapping catalytic sites in $RuMoS_{2+x}$ cocatalysts for efficient alkaline photocatalytic H_2 production, Appl. Catal. B Environ. 319 (2022) 121910.

[7] L. Liu, H. Meng, Y. Chai, X. Chen, J. Xu, X. Liu, W. Liu, D.M. Guldi, Y. Zhu, Enhancing built-in electric fields for efficient photocatalytic hydrogen evolution by encapsulating C_{60} fullerene into zirconium-based metal-organic frameworks, Angew. Chem. Int. Ed. 62 (2023) e202217897.

[8] H. Long, D. Gao, P. Wang, X. Wang, F. Chen, H. Yu, Amorphization-induced reverse electron transfer in NiB cocatalyst for boosting photocatalytic H_2 production, Appl. Catal. B Environ. 340 (2024) 123270.

[9] L. Wang, G. Tang, S. Liu, H. Dong, Q. Liu, J. Sun, H. Tang, Interfacial active-site-rich 0D Co_3O_4/1D TiO_2 p-n heterojunction for enhanced photocatalytic hydrogen evolution, Chem. Eng. J. 428 (2022) 131338.

[10] W. Zhong, B. Zhao, X. Wang, P. Wang, H. Yu, Synchronously enhancing water adsorption and strengthening Se–H_{ads} bonds in Se-Rich $RuSe_{2+x}$ cocatalyst for efficient alkaline photocatalytic H_2 production, ACS Catal. 13 (2023) 749–756.

[11] D. Liu, B. Sun, S. Bai, T. Gao, G. Zhou, Dual co-catalysts $Ag/Ti_3C_2/TiO_2$ hierarchical flower-like microspheres with enhanced photocatalytic H_2-production activity, Chin. J. Catal. 50 (2023) 273–283.

[12] M. Wang, P. Wang, X. Wang, F. Chen, H. Yu, Self-optimized H-adsorption affinity of CuRu alloy cocatalysts towards efficient photocatalytic H_2 evolution, J. Mater. Sci. Technol. 174 (2024) 168–175.

[13] Y. Yamazaki, T. Toyonaga, N. Doshita, K. Mori, Y. Kuwahara, S. Yamazaki, H. Yamashita, Crystal facet engineering and hydrogen spillover-assisted synthesis of defective Pt/TiO_{2-x} nanorods with enhanced visible light-driven photocatalytic activity, ACS Appl. Mater. Interfaces 14 (2022) 2291–2300.

[14] J. He, L. Hu, C. Shao, S. Jiang, C. Sun, S. Song, Photocatalytic H_2O overall splitting into H_2 bubbles by single atomic sulfur vacancy CdS with spin polarization electric field, ACS Nano 15 (2021) 18006–18013.

[15] J. Xu, W. Zhong, D. Gao, X. Wang, P. Wang, H. Yu, Phosphorus-enriched platinum diphosphide nanodots as a highly efficient cocatalyst for photocatalytic H_2 evolution of CdS, Chem. Eng. J. 439 (2022) 135758.

[16] T. Di, Q. Deng, G. Wang, S. Wang, L. Wang, Y. Ma, Photodeposition of CoO_x and MoS_2 on CdS as dual cocatalysts for photocatalytic H_2 production, J. Mater. Sci. Technol. 124 (2022) 209–216.

[17] M. Zhao, S. Liu, D. Chen, S. Zhang, S.A.C. Carabineiro, K. Lv, A novel S-scheme 3D $ZnIn_2S_4/WO_3$ heterostructure for improved hydrogen production under visible light irradiation, Chin. J. Catal. 43 (2022) 2615–2624.

[18] J. Xu, W. Zhong, F. Chen, X. Wang, H. Yu, In situ cascade growth-induced strong coupling effect toward efficient photocatalytic hydrogen evolution of $ReS_2/ZnIn_2S_4$, Appl. Catal. B Environ. 328 (2023) 122493.

[19] W. Huang, Z. Li, C. Wu, H. Zhang, J. Sun, Q. Li, Delaminating Ti_3C_2 MXene by blossom of $ZnIn_2S_4$ microflowers for noble-metal-free photocatalytic hydrogen production, J. Mater. Sci. Technol. 120 (2022) 89–98.

[20] J. Xu, L. Wang, L. Sun, W. Wang, T. Kong, H. Jiang, Q. Liu, Boosting photocatalytic synchronous production of H_2 coupled with acetone over Co doped Cu_3P quantum dots/$ZnIn_2S_4$ nanosheets p-n nanojunction, J. Colloid Interface Sci. 646 (2023) 254–264.

[21] Y. Huang, F. Mei, J. Zhang, K. Dai, G. Dawson, Construction of 1D/2D $W_{18}O_{49}$/porous g-C_3N_4 S-scheme heterojunction with enhanced photocatalytic H_2 evolution, Acta Phys. Chim. Sin. 38 (2022) 2108028.

[22] Z. Xie, Q. Gao, S. Hussain, J. Yang, Q. Li, Supermolecule polymer derived porous carbon nitride microspheres with controllable energy band structure for photocatalytic hydrogen evolution reaction, Small (2023) 2309032.

[23] Y. Hu, X. Yu, Q. Liu, L. Wang, H. Tang, Highly metallic Co-doped MoS_2 nanosheets as an efficient cocatalyst to boost photoredox dual reaction for H_2 production and benzyl alcohol oxidation, Carbon 188 (2022) 70–80.

[24] X. Wu, L. Tan, G. Chen, J. Kang, G. Wang, g-C_3N_4-based S-scheme heterojunction photocatalysts, Sci. China Mater. 67 (2024) 444–472.

[25] F. Li, X. Yue, Y. Liao, L. Qiao, K. Lv, Q. Xiang, Understanding the unique S-scheme charge migration in triazine/heptazine crystalline carbon nitride homojunction, Nat. Commun. 14 (2023) 3901.

[26] J. Xu, D. Gao, H. Yu, P. Wang, B. Zhu, L. Wang, J. Fan, Palladium-copper nanodot as novel H_2-evolution cocatalyst: optimizing interfacial hydrogen desorption for highly efficient photocatalytic activity, Chin. J. Catal. 43 (2022) 215–225.

[27] D. Tang, C. Shao, S. Jiang, C. Sun, S. Song, Graphitic C_2N_3: An allotrope of g-C_3N_4 containing active azide pentagons as metal-free photocatalyst for abundant H_2 bubble evolution, ACS Nano 15 (2021) 7208–7215.

[28] Y.-D. Wang, T.-W. Lee, Y.-C. Lo, W.-J. Hong, C. Chen, Insights into photochemical stability of graphitic carbon nitride-based photocatalysts in water treatment, Carbon 175 (2021) 223–232.

[29] H. Dong, L. Tong, P. Zhang, D. Zhu, J. Jiang, C. Li, Built-in electric field intensified by photothermoelectric effect drives charge separation over Z-scheme 3D/2D In_2Se_3/PCN heterojunction for high-efficiency photocatalytic CO_2 reduction, J. Mater. Sci. Technol. 179 (2024) 251–261.

[30] C. Qiu, Y. Xu, X. Fan, D. Xu, R. Tandiana, X. Ling, Y. Jiang, C. Liu, L. Yu, W. Chen, C. Su, Highly crystalline K-intercalated polymeric carbon nitride for visible-light photocatalytic alkenes and alkynes deuterations, Adv. Sci. 6 (2019) 1801403.

[31] G. Zhang, Y. Xu, D. Yan, C. He, Y. Li, X. Ren, P. Zhang, H. Mi, Construction of K^+ ion gradient in crystalline carbon nitride to accelerate exciton dissociation and charge separation for visible light H_2 production, ACS Catal. 11 (2021) 6995–7005.

[32] B. Zhao, W. Zhong, F. Chen, P. Wang, C. Bie, H. Yu, High-crystalline g-C_3N_4 photocatalysts: synthesis, structure modulation, and H_2-evolution application, Chin. J. Catal. 52 (2023) 127–143.

[33] G. Huang, B. Xiao, L. Bao, D. Wang, Y. Luo, S. Yan, H. Gao, Crystalline oxygen-bridged carbon nitride from self-assembled supramolecular intermediate for efficient photocatalytic H_2 evolution, J. Mater. Chem. A 12 (2024) 3480–3488.

[34] H. Guo, C.-G. Niu, C. Liang, H.-Y. Niu, Y.-Y. Yang, H.-Y. Liu, N. Tang, H.-X. Fang, Highly crystalline porous carbon nitride with electron accumulation capacity: promoting exciton dissociation and charge carrier generation for photocatalytic molecular oxygen activation, Chem. Eng. J. 409 (2021) 128030.

[35] X. Wu, H. Ma, K. Wang, J. Wang, G. Wang, H. Yu, High-yield and crystalline graphitic carbon nitride photocatalyst: one-step sodium acetate-mediated synthesis and improved hydrogen-evolution performance, J. Colloid Interface Sci. 633 (2023) 817–827.

[36] F. Guo, B. Hu, C. Yang, J. Zhang, Y. Hou, X. Wang, On-surface polymerization of in-plane highly ordered carbon nitride nanosheets toward photocatalytic mineralization of mercaptan gas, Adv. Mater. 33 (2021) 2101466.

[37] Q. Li, Y. Jiao, Y. Tang, J. Zhou, B. Wu, B. Jiang, H. Fu, Shear stress triggers ultrathin-nanosheet carbon nitride assembly for photocatalytic H_2O_2 production coupled with selective alcohol oxidation, J. Am. Chem. Soc. 145 (2023) 20837–20848.

[38] S. Yan, Y. Li, X. Yang, X. Jia, J. Xu, H. Song, Photocatalytic H_2O_2 generation reaction with a benchmark rate at air-liquid-solid joint interfaces, Adv. Mater. 36 (2024) 2307967.

[39] W. Wang, H. Zhang, Y. Chen, H. Shi, Efficient degradation of tetracycline via coupling of photocatalysis and photo-fenton processes over a 2D/2D α-Fe_2O_3/g-C_3N_4 S-scheme heterojunction catalyst, Acta Phys. Chim. Sin. 38 (2022) 2201008.

[40] D. Yang, Z. Liu, P. Yang, L. Huang, F. Huang, X. Tao, Y. Shi, R. Lei, J. Cao, H. Li, X. Chen, Z. Bian, A curtain purification system based on a rabbit fur-based rotating triboelectric nanogenerator for efficient photocatalytic degradation of volatile organic compounds, Nanoscale 15 (2023) 6709–6721.

[41] C. Li, P. Zhang, F. Gu, L. Tong, J. Jiang, Y. Zuo, H. Dong, Atomically dispersed Au confined by oxygen vacancies in Au-θ-Al_2O_3/Au/PCN hybrid for boosting photocatalytic CO_2 reduction driven by multiple built-in electric fields, Chem. Eng. J. 476 (2023) 146514.

[42] Z.-K. Xie, Y.-J. Jia, Y.-Y. Huang, D.-B. Xu, X.-J. Wu, M. Chen, W.-D. Shi, Near-infrared light-driven photocatalytic reforming lignocellulose into H_2 and chemicals over heterogeneous carbon nitride, ACS Catal. 13 (2023) 13768–13776.

[43] B. Zhao, D. Gao, W. Zhong, F. Chen, P. Wang, X. Wang, H. Yu, Highly intra- and inter-plane crystalline ReS_x/g-C_3N_4: facile synthesis and boosted photocatalytic H_2 evolution, Chem. Eng. J. 479 (2024) 147711.

[44] F. He, Y. Lu, Y. Wu, S. Wang, Y. Zhang, P. Dong, Y. Wang, C. Zhao, S. Wang, J. Zhang, S. Wang, Rejoint of carbon nitride fragments into multi-interfacial order-disorder homojunction for robust photo-driven generation of H_2O_2, Adv. Mater. 36 (2024) 2307490.

[45] G. Zhang, Y. Xu, J. Zhu, Y. Li, C. He, X. Ren, P. Zhang, H. Mi, Enhanced photocatalytic H_2 production independent of exciton dissociation in crystalline carbon nitride, Appl. Catal. B Environ. 338 (2023) 123049.

[46] X. Han, Y. Kang, S. Song, R. Lu, A. Yu, Sodium ion doped graphitic carbon nitride with high crystallinity for superior photocatalytic hydrogen evolution efficiency, J. Mater. Chem. A 11 (2023) 18213–18226.

[47] X. Li, J. Wu, S. An, K. Li, J. Zhang, M. Pei, C. Song, X. Guo, Ultrathin crystalline carbon nitride nanosheets for highly efficient photocatalytic pollutant removal and hydrogen production, ACS Appl. Nano Mater. 6 (2023) 11601–11611.

[48] H. Huang, K. Xiao, N. Tian, F. Dong, T. Zhang, X. Du, Y. Zhang, Template-free precursor-surface-etching route to porous, thin g-C_3N_4 nanosheets for enhancing photocatalytic reduction and oxidation activity, J. Mater. Chem. A 5 (2017) 17452–17463.

[49] K. Mori, H. Hata, H. Yamashita, Interplay of Pd ensemble sites induced by GaO_x modification in boosting CO_2 hydrogenation to formic acid, Appl. Catal. B Environ. 320 (2023) 122022.

[50] E. Hu, Q. Chen, Q. Gao, X. Fan, X. Luo, Y. Wei, G. Wu, H. Deng, S. Xu, P. Wang, L. Liu, R. He, X. Chen, W. Zhu, Y. Zhu, Cyano-functionalized graphitic carbon

nitride with adsorption and photoreduction isosite achieving efficient uranium extraction from seawater, Adv. Funct. Mater. (2024) 2312215.

[51] K. Li, W. Zhou, X. Li, Q. Li, S.A.C. Carabineiro, S. Zhang, J. Fan, K. Lv, Synergistic effect of cyano defects and $CaCO_3$ in graphitic carbon nitride nanosheets for efficient visible-light-driven photocatalytic NO removal, J. Hazard. Mater. 442 (2023) 130040.

[52] Y. Jiang, S. Fang, C. Cao, E. Hong, L. Zeng, W. Yang, L. Huang, C. Yang, Enhanced light harvesting and charge separation of carbon and oxygen co-doped carbon nitride as excellent photocatalyst for hydrogen evolution reaction, J. Colloid Interface Sci. 612 (2022) 367–376.

[53] Z. Lian, F. Gao, H. Xiao, D. Luo, M. Li, D. Fang, Y. Yang, J. Zi, H. Li, Photo-self-fenton reaction mediated by atomically dispersed Ag−Co photocatalysts toward efficient degradation of organic pollutants, Angew. Chem. Int. Ed. 63 (2024) e202318927.

[54] L. Chen, F. Wang, J. Zhang, H. Wei, L. Dang, The preserved S-scheme band structure of graphitic carbon nitride/bismuth oxobromide after the introduction of black phosphorus driven by an internal electric field: achieving significantly enhanced photocatalytic performance, J. Mater. Chem. A 11 (2023) 26086–26104.

[55] Z. Lei, X. Ma, X. Hu, J. Fan, E. Liu, Enhancement of photocatalytic H_2-evolution kinetics through the dual cocatalyst activity of Ni_2P-NiS-decorated g-C_3N_4 heterojunctions, Acta Phys. Chim. Sin. 38 (2022) 2110049.

[56] Q. Zhang, X. Chen, Z. Yang, T. Yu, L. Liu, J. Ye, Precisely tailoring nitrogen defects in carbon nitride for efficient photocatalytic overall water splitting, ACS Appl. Mater. Interfaces 14 (2022) 3970–3979.

[57] S. Hu, D. Jiang, L. Gu, G. Xu, Z. Li, Y. Yuan, Awakening n → π* electronic transition by breaking hydrogen bonds in graphitic carbon nitride for increased photocatalytic hydrogen generation, Chem. Eng. J. 399 (2020) 125847.

[58] D. Yuan, X. Chen, Z. Li, C. Fang, J. Ding, H. Wan, G. Guan, The impact of benzene ring embedding on the performance of carbon nitride for photocatalytic hydrogen, Appl. Surf. Sci. 569 (2021) 151089.

[59] D. Gao, J. Xu, F. Chen, P. Wang, H. Yu, Unsaturated selenium-enriched $MoSe_{2+x}$ amorphous nanoclusters: One-step photoinduced co-reduction route and its boosted photocatalytic H_2-evolution activity for TiO_2, Appl. Catal. B Environ. 305 (2022) 121053.

[60] Z. Yu, X. Yue, J. Fan, Q. Xiang, Crystalline intramolecular ternary carbon nitride homojunction for photocatalytic hydrogen evolution, ACS Catal. 12 (2022) 6345–6358.

[61] D. Gao, H. Long, X. Wang, J. Yu, H. Yu, Tailoring antibonding-orbital occupancy state of selenium in Se-enriched $ReSe_{2+x}$ cocatalyst for exceptional H_2 evolution of TiO_2 photocatalyst, Adv. Funct. Mater. 33 (2023) 2209994.

[62] Z. Zhang, L. Ren, H. Li, D. Jiang, Y. Fang, H. Du, G. Xu, C. Zhu, H. Li, Z. Lu, Y. Yuan, π-conjugated in-plane heterostructure enables long-lived shallow trapping in graphitic carbon nitride for increased photocatalytic hydrogen generation, Small 19 (2023) 2207173.

[63] D. Gao, W. Zhong, X. Zhang, P. Wang, H. Yu, Free-electron inversive modulation to charge antibonding orbital of ReS_2 cocatalyst for efficient photocatalytic hydrogen generation, Small 20 (2024) 2309123.